



HAL
open science

Identification of the Bandwidth of a Magneto-Inertial Navigation Filter

Raphaël Neymann, Mathieu Hillion, Hugo Lhachemi, Christophe Prieur,
Antoine Girard

► **To cite this version:**

Raphaël Neymann, Mathieu Hillion, Hugo Lhachemi, Christophe Prieur, Antoine Girard. Identification of the Bandwidth of a Magneto-Inertial Navigation Filter. MICNON 2024 - 4th IFAC Conference on Modelling, Identification and Control of Nonlinear Systems, IFAC, Sep 2024, Lyon, France. hal-04642739

HAL Id: hal-04642739

<https://hal.science/hal-04642739v1>

Submitted on 10 Jul 2024

HAL is a multi-disciplinary open access archive for the deposit and dissemination of scientific research documents, whether they are published or not. The documents may come from teaching and research institutions in France or abroad, or from public or private research centers.

L'archive ouverte pluridisciplinaire **HAL**, est destinée au dépôt et à la diffusion de documents scientifiques de niveau recherche, publiés ou non, émanant des établissements d'enseignement et de recherche français ou étrangers, des laboratoires publics ou privés.

Identification of the Bandwidth of a Magneto-Inertial Navigation Filter

Raphaël Neymann^{*,**} Mathieu Hillion^{**} Hugo Lhachemi^{*}
Christophe Prieur^{***} Antoine Girard^{*}

^{*} *Université Paris-Saclay, CNRS, CentraleSupélec, Laboratoire des Signaux et Systèmes, 91190 Gif-sur-Yvette, France.*

^{**} *SYSNAV, 27200 Vernon, France.*

^{***} *Université Grenoble Alpes, CNRS, Grenoble-INP, GIPSA- lab, 38000 Grenoble, France.*

Abstract:

We address the analysis of a nonlinear navigation filter used in Magneto-Inertial Dead-Reckoning (MIDR) whose input data are provided by a home-made device. This filter takes the measurements given by the magnetic sensors as inputs and returns the velocity of the body. Therefore, any unmodeled time-varying disturbance in the measurements impacts the estimation of the velocity and yields errors that distort the estimation. For dimensioning purpose, we aim to identify the bandwidth of the linearized part of this filter. To derive a model of this bandwidth, we first simplify our filter as a time-invariant Single-Input Single-Output (SISO) system in the situation where the steady-state regime is reached. The Best Linear Approximation (BLA) of this nonlinear system can hence be described by a conventional transfer function. We justify the validity of such a linear approximation for Extended Kalman Filters (EKF) and identify it with different methods, yielding a model for the bandwidth depending on the experimental conditions of navigation. We show that our filter is actually suitable for pedestrian navigation. Finally, simulations in realistic physical situations are used for validation.

Keywords: Calibration, Dead-Reckoning, Experimental Settings, Magnetic Navigation, Model Validation, Nonlinear Systems, Statistical Analysis, Volterra Series, Time Series Analysis.

1. INTRODUCTION

Filtering sensors data is used in navigation for estimating the displacement of a rigid body. In particular, Magneto-Inertial Dead-Reckoning (MIDR) is a category of algorithms relying on the addition of the equation of magnetism in the filter, *e.g.* an Extended Kalman Filters (EKF). To this extent, Magneto-Inertial Measurement Units (MIMU), consisting in the combination of an inertial unit and an array of magnetic sensors are used as hardware devices for recording the data (Vissière et al. (2007); Chesneau et al. (2016)). With known geometry, the measurements of this array allow to compute both local average magnetic field and Jacobian matrix – the *magnetic gradient*. This magnetic gradient is crucial in the estimation of the velocity, since it conditions its observability, and increases the signal-to-noise ratio (SNR).

This navigation technology is particularly used for indoor pedestrian navigation (Zmitri et al. (2021); Neymann et al. (2023a)), since space variations of the magnetic field are there mostly available. However, indoor environments are also subject to many time-varying electromagnetic perturbations. Some undesired and unmodelizable events – *e.g.* opening doors, air conditioning pulses, or to a lesser extent power-line interferences (Chesneau et al. (2016)) – are high frequency (HF) phenomena that significantly disturb the navigation performances. Lower frequencies disturbances – *e.g.* calibration errors (Chesneau et al.

(2016, 2019); Neymann et al. (2023b)) – also alter the estimation. Furthermore, MIMU are facing industrial challenges as systems tend to be miniaturized. This seek to miniaturization firstly consists in making the device more wearable or ergonomic, but also implies many changes in the electronics, *e.g.* changing the sampling rate.

In this paper, we are interested in well sizing a MIMU and its MIDR filter to determine the best setting for a more accurate pedestrian navigation. Given the size of the MIMU, and its sampling rate, we aim to characterize its response in velocity to unmodeled time-varying magnetic disturbances by determining a bandwidth. The knowledge of this bandwidth is crucial for classifying naturally filtered disturbances and those that decrease the navigation performances. Another important point is miniaturization: having a model of the filter with respect to the hardware parameters allows to predict the expected navigation performances, and conversely to tune these parameters. Moreover, since velocity and gradient are closely tied, it is important to link the behavior with different velocity-gradient trajectory scenarii.

The identification of a filter bandwidth needs the knowledge of a Single-Input Single Output (SISO) linear system. Since a MIDR algorithm inputs the calibrated multidimensional magnetic measurements of the sensors array and outputs a 3D velocity, we first consider a simplified 1D MIDR algorithm, which outputs a scalar velocity and in-

puts the measurements of two parallel scalar magnetometers whose only one is disturbed. Given this SISO nonlinear system and assuming a steady-state regime, we identify its Best Linear Approximation (BLA) (Schoukens and Ljung (2019)). We prefer a kernel-based strategy (Rugh (1981)) rather than a block-oriented approach (Schoukens and Tiels (2017)), since a first order kernel directly provides the BLA and consequently its time constants.

The remaining of this paper is organized as follows: we first recall the basics of an MIDR-EKF and derive a 1D toy-model, yielding a simple SISO system. This toy-model is useful for understanding the physical behavior of the dynamic system with respect to the input parameters: sample rate, size of the device, and the values of the velocity and the magnetic gradient (Section 2). We thereafter provide some results about expansion in Volterra kernels for linear time-invariant (LTI) systems and prove that this decomposition is justified for EKF (Section 3). We then derive a simulated model of the BLA of this SISO system for diverse velocities or magnetic gradients (Section 4). Finally, the model is challenged with simulated but realistic three-dimensional trajectories and validated in these real-life use cases (Section 5).

2. MAGNETO-INERTIAL DEAD-RECKONING EXTENDED KALMAN FILTER (MIDR-EKF)

We recall in this section the basic knowledges about MIDR-EKF, as it was first established in Vissière et al. (2007), as well as the 1D MIDR-EKF toy-model from Neymann et al. (2023a), and define the filter to identify.

2.1 Classic MIDR-EKF

In this paper, we denote by \mathbf{B} the *magnetic flux density*, expressed in $1 \text{ G} = 10^{-4} \text{ kg} \cdot \text{A}^{-1} \cdot \text{s}^{-2}$. Moreover, a vector $\mathbf{u}^n = \mathbf{R}\mathbf{u}^b \in \mathbb{R}^3$ in the navigation frame is denoted with an upperscript (n), whereas (b) denotes the body frame, with $\mathbf{R} \in \text{SO}_3(\mathbb{R})$ is a rotation matrix. The rotation rate, provided by the gyrometer, is a skew-symmetric matrix $\mathbf{\Omega}^{b/n} \in \mathfrak{so}_3(\mathbb{R})$, the tangent space of $\text{SO}_3(\mathbb{R})$.

The classic MIDR-EKF consists in a usual inertial filter with a magnetic correction through equation

$$\dot{\mathbf{B}}^b(t) = -\mathbf{\Omega}^{b/n}(t)\mathbf{B}^b(t) + \nabla\mathbf{B}^b(t)\mathbf{v}^b(t), \quad (1)$$

where $\nabla\mathbf{B}^b$ denotes the – stationar – Jacobian matrix – gradient – of the magnetic field, and \mathbf{v}^b the velocity.

2.2 Measurements of a 1D magnetometers array

Consider a scalar displacement along the coordinate x , on which a stationar magnetic field $B(x)$ is defined. Neymann et al. (2023a) simplified the MIMU with two parallel and aligned single-axis magnetometers 1 and 2 referenced from the origin of the device by algebraic distances p_1 and p_2 , *s.t.* the size of the MIMU is $p_2 - p_1$. At each timestamp $k\Delta t$, the calibrated measurement of the i -th magnetometer is given by $M_{i,k} \in \mathbb{R}$, which corresponds to the actual magnetic field $B(x_k + p_i) + \nu_{i,k}$ at the position $x_k = x(k\Delta t)$ where $\nu_{i,k} \sim \mathcal{N}(0, \sigma_{\text{mag}}^2)$. The average field is computed as $B_k = (p_2 M_{1,k} - p_1 M_{2,k}) / (p_2 - p_1)$ and the gradient as $\lambda_k = (M_{2,k} - M_{1,k}) / (p_2 - p_1)$. The coefficient

$\rho = \sqrt{(p_2 - p_1)^2 / (p_1^2 + p_2^2)}$ allows to define the *saturation velocity* as $v_0 = \rho(p_2 - p_1) / (2\Delta t)$: the maximal velocity that can be processed by the filter, *i.e.* the velocity of the body moving from its own size during the inverse of the Shannon frequency $f_{\text{sh}} = 1 / (2\Delta t)$.

2.3 Design of a 1D study filter

From Neymann et al. (2023a), we recall the velocity \hat{v}_k and magnetic field \hat{B}_k estimator Kalman filter given by

$$\begin{pmatrix} \hat{v}_{k+1|k} \\ \hat{B}_{k+1|k} \end{pmatrix} = \begin{pmatrix} 1 & 0 \\ \lambda_k \Delta t & 1 \end{pmatrix} \begin{pmatrix} \hat{v}_{k|k} \\ \hat{B}_{k|k} \end{pmatrix} + \begin{pmatrix} \Delta t \\ \frac{1}{2} \lambda_k \Delta t^2 \end{pmatrix} \gamma^k \quad (2)$$

$$B_k = \hat{B}_{k|k}$$

where γ_k denotes the proper acceleration provided by an (unbiased) accelerometer over the period $(k\Delta t, (k+1)\Delta t)$.

The nonlinearity of the filter comes from the cross term $\lambda_k \hat{v}_{k|k}$ in (2), since the computation of the gradient derives from the difference of magnetic measurements, the gradient is also altered by any disturbance.

2.4 Considered Filter in this Study

The filter (2) of Section 2.3 does not model potential nongaussian time-dependent measurement disturbances. Therefore, we aim to identify the bandwidth of the BLA of the SISO system

$$(\Delta M_{1,k})_{k \geq 0} \mapsto (\Delta v_k)_{k \geq 0} \quad (3)$$

where $\Delta M_{1,k}$ is the disturbance in $M_{1,k}$ and Δv_k the estimation error in \hat{v} .

Low frequencies situations are not detailed in this paper. Indeed the authors of Neymann et al. (2023a) already derived from (2) the error in the velocity due to a static measurement error ΔM – *e.g.* wrong calibration:

$$\Delta v / v = -\Delta M / [\lambda(p_2 - p_1)] = -\Delta \lambda / \lambda, \quad (4)$$

where $\Delta \lambda = \Delta M / (p_2 - p_1)$ is the error in the gradient.

3. VOLTERRA KERNELS AND KALMAN FILTERS

After providing elements about expansion in Volterra kernels for SISO-LTI systems, we extend this decomposition for linearized steady-state EKF under the assumption of a finite fading memory of length $m \geq 1$.

3.1 Theory overview

For discretized systems, a version of the decomposition in Volterra kernels can be derived (Schetzen (1980)). For the sake of simplicity, assume that this expansion is made at the second order, which reads

$$y_k = h^0 + \sum_{k_1=0}^{m-1} h_{k_1}^1 u_{k-k_1} + \sum_{k_1=0}^{m-1} \sum_{k_2=0}^{m-1} h_{k_1, k_2}^2 u_{k-k_1} u_{k-k_2}, \quad (5)$$

where h^i is the i -th order kernel of the expansion and m is the length of the finite-time memory – supposed shared for all discretized kernels. The constant zeroth kernel h^0 denotes the offset of the system. The first kernel h^1 is exactly the BLA (Schoukens and Ljung (2019)). Its Fourier Transform is exactly the transfer function of the linearized

filter. Moreover, the second kernel h^2 depicts the time cross-correlations, and extends to higher orders $i > 2$.

This expansion is only valid over a compact subset of the input signals. In practice, the fading memory hypothesis makes of any bounded perturbation subset a valid compact subset for the norm defined in Boyd and Chua (1985).

Theorem 1. Continuity of the Volterra kernels.

Let $n \geq 1$ and $m \geq 1$ be the maximal order of the Volterra expansion and the length of the memory. Moreover, let $(u_k)_{k \geq 0}$ be a scalar bounded sequence, i.e. $\|u\|_\infty = \sup_{k \geq 0} |u_k| < \infty$. Then the response $(y_k)_{k \geq 0}$ to the n -th order Volterra expansion is bounded and satisfies

$$\|y\|_\infty \leq \sum_{i=0}^n \|h^i\|_1 \|u\|_\infty^i, \quad \|h^i\|_1 = \sum_{k_1, \dots, k_i}^{m-1} |h_{k_1, \dots, k_i}^i|. \quad (6)$$

The regularity of Volterra kernels hence controls the response of the filter to a given input. In this paper, we restrict the analysis to second order expansions.

3.2 Kernels for Kalman Filters

Kalman filtering is used when noisy data have to be integrated, and relies on the following state-space representation (Anderson and Moore (1979))

$$\mathbf{x}_{k+1|k} = \mathbf{F}_k \mathbf{x}_{k|k} + \mathbf{G}_k \mathbf{u}_k, \quad \mathbf{y}_k = \mathbf{H}_k \mathbf{x}_k, \quad (7)$$

where $\mathbf{x}_{k|k}$, $\mathbf{x}_{k+1|k} \in \mathbb{R}^n$ are the corrected and predicted states, $\mathbf{u}_k \in \mathbb{R}^m$ is the input, $\mathbf{y}_k \in \mathbb{R}^p$ is the observation. Matrices $\mathbf{F}_k \in \mathbb{R}^{n \times n}$, $\mathbf{G}_k \in \mathbb{R}^{n \times m}$ and $\mathbf{H}_k \in \mathbb{R}^{p \times n}$ are respectively the transition, the input transfers and observation matrices. The correction is achieved by an outer measurement $\mathbf{z}_k \in \mathbb{R}^p$.

In this section, we analyze the transfer from \mathbf{z}_k to $\mathbf{x}_{k|k}$. In particular, we prove that the transfer from an error in \mathbf{z}_k to an error in $\mathbf{x}_{k|k}$ can be approximated at first order in a steady-state regime by a LTI system. Recalling that the transfer of (3) is SISO, we prove that a SISO transfer derives from this LTI system.

The case of LTI systems is easily achieved with a Wiener approach (Radix (1993)) or by taking the z -transform of the transfer from \mathbf{z}_k to $\mathbf{x}_{k|k}$ for $z = e^{i2\pi f \Delta t}$, which reads:

$$\mathcal{H}_{\text{LTI}}(z) = z^{-1} [\mathbf{I} - z^{-1} (\mathbf{F} - \mathbf{K}\mathbf{H}^\top)]^{-1} \mathbf{K} \in \mathbb{R}^{n \times p}, \quad (8)$$

where $\mathbf{K} \in \mathbb{R}^{n \times p}$ is the Kalman gain matrix. In the case of EKF, the matrices \mathbf{F}_k , \mathbf{H}_k , and \mathbf{K}_k may depend on the measurements and are then disturbed by perturbations in the data and the previous technique no longer applies. Hence, the error of estimation should be taken in expected value, i.e. $\Delta \mathbf{x}_k = \mathbb{E}[\hat{\mathbf{x}}_{k|k} - \bar{\mathbf{x}}_k]$, where $\hat{\mathbf{x}}_{k|k}$ is the estimated state and $\bar{\mathbf{x}}_k$ the actual state.

Theorem 2. Dynamic of the error of estimation.

The estimation of error has the following dynamic:

$$\Delta \mathbf{x}_{k+1} = (\mathbf{I} - \mathbf{K}_{k+1} \mathbf{H}_k^\top) \mathbf{F}_{k+1} \Delta \mathbf{x}_k + \mathbf{K}_{k+1} \Delta \mathbf{z}_{k+1}, \quad (9)$$

where \mathbf{K}_k is the Kalman gain and $\Delta \mathbf{z}_k = \mathbb{E}[\mathbf{z}_k - \mathbf{H}_k \bar{\mathbf{x}}_k]$.

Proof 1. The reader may refer to App. A.

Assuming that $\Delta \mathbf{x}_0 = \mathbf{0}$ – i.e. the state is initially well estimated in average – and that $\Delta \mathbf{z}_k$ has finite support, a recursion provides

$$\Delta \mathbf{x}_k = \sum_{i=0}^{+\infty} \mathbf{h}_{k,i} \Delta \mathbf{z}_{k-i} = (\mathbf{h}_k * \Delta \mathbf{z}_k), \quad (10)$$

with $\mathbf{h}_{k,i} = \left[\prod_{j=0}^{i-1} (\mathbf{I} - \mathbf{K}_{k-j} \mathbf{H}_k^\top) \mathbf{F}_{k-j} \right] \mathbf{K}_{k-i} \in \mathbb{R}^{n \times p}$.

This result is a convolution formula between the first order time-variant matrix kernel $\mathbf{h}_k : i \mapsto \mathbf{h}_{k,i}$ – which naturally includes the transient period of the Kalman filter – and the input perturbation $\Delta \mathbf{z}_k$ – i.e. the innovation relatively to the actual state – corresponding to the input u_k in the Volterra expansion of (5), whereas y_k is there replaced by $\Delta \mathbf{x}_k$.

Yet, the system is still not LTI-SISO. In a steady-state regime, and assuming that the matrices are inputs-independent, all the indices k drop out and one can take the z -transform of (9), yielding the LTI transfer matrix from $\Delta \mathbf{z}_k$ to $\Delta \mathbf{x}_k$:

$$\mathcal{H}(z) = [\mathbf{I} - z^{-1} (\mathbf{I} - \mathbf{K}\mathbf{H}^\top) \mathbf{F}]^{-1} \mathbf{K} \in \mathbb{R}^{n \times p}. \quad (11)$$

The time constants of the filter are fully determined by the eigenvalues of the square matrix $(\mathbf{I} - \mathbf{K}\mathbf{H}^\top) \mathbf{F}$, whose spectral radius must be < 1 to ensure the stability of the system. We hence derived a LTI first order response. However, this transfer is multidimensional and not SISO. Finally, extracting a SISO subsystem from (11) is componentwisely achieved by taking $\mathcal{H}_{ij}(z)$.

4. IDENTIFICATION OF THE MIDR-EKF

In this section, we identify the bandwidth of (3) by computing the BLA in the framework of Section 2. We simulated straight line trajectories with constant velocities v and magnetic gradient λ , s.t. $B(x) = B_0 + \lambda x$. Only the measurements M_1 of magnetometer 1 were disturbed. We also showed that, once the steady-state regime reached, the expansion in Volterra kernels is equivalent to (11).

4.1 Implementation of the computation of Volterra kernels

The measurements of magnetometer 1 were excited with a centered gaussian noise ΔM_k of variance $\sigma_{\text{mag}}^2 = (1 \text{ mG})^2$. This input signal excites all the frequencies and is time-decorrelated. The simulations lasted 180 s and the kernels were identified with a finite memory of 12 s from $t_0 = 60$ s, after the convergence of the EKF. The Volterra kernels were identified with order phase separations (Bouvier et al. (2017)). Compared with other algorithms (Birpoutsoukis et al. (2017, 2018)), the phases separations are more resilient to actual signal without *a priori*. For comparison, we also implemented (10).

4.2 Validity of a linear approximation of the MIDR-EKF

The identification yields an offset h^0 which numerically equals $0 \text{ m} \cdot \text{s}^{-1}$, i.e. the MIDR-EKF is an unbiased filter. The first order h^1 was processed and compared to the theoretical kernel from (10) (Fig. 1). Both estimations are equivalent up to $\sim 20 \cdot 10^{-6}$ in maximum, which impacts the estimation of the velocity with a negligible disturbance of $\sim 10^{-8} \text{ m} \cdot \text{s}^{-1}$, so both methods are equivalent. Moreover, we identified $\|h^2\|_\infty \approx 10^{-5} \text{ m} \cdot \text{s}^{-1} \cdot \text{G}^{-2}$, which is also negligible since the related error in velocity is

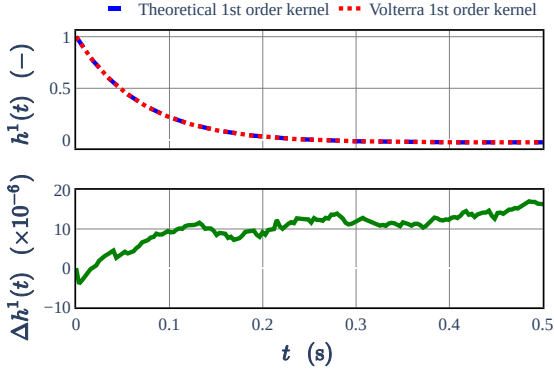


Fig. 1. Theoretical and Volterra normalized 1st order kernels are numerically identical up to a maximal difference under $20 \cdot 10^{-6}$.

$\sim 10^{-11} \text{ m} \cdot \text{s}^{-1}$. Consequently, the MIDR-EKF can be approximated by a first linear filter with impulsional response h^1 . In the Fourier space, the filter can be modeled by $\mathcal{F}(\Delta v)(f) = H^1(f)\mathcal{F}(\Delta M)(f)$, where f is the frequency of the input and $H^1(f) = \mathcal{F}(h^1)(f)$.

4.3 Model for the MIDR-EKF

We now aim to characterize the Bode plot of H^1 depending on the trajectory scenario (v, λ) . We process the impulsional response $h^1(t)$ for different scenarios, providing different BLA of the filter. We compute the gain as $G(f) = 20 \log |H^1(f)/H_0^1|$, where H_0^1 is a normalization factor defined such that $\max_{f \in (0, f_{\text{sh}})} G(f) = 0 \text{ dB}$, and the phase is $\phi(f) = \arg H^1(f)$. The complete Bode plots for a complete batch of trajectories are provided on Fig. 2. The general shape of the filter is band-pass¹, which is consistent with the fact that static errors in the measurements are already modeled by (4). The global slopes of the gain are +20 dB and -20 dB per decade, which respectively correspond to a real zero and a real pole. Moreover, the phase ϕ cancels at the upper cutting frequency, and tends to $\pi/2$ as f goes to 0 Hz. The lower and upper cutting frequencies f_{low} and f_{up} are computed such that $G(f) = -3 \text{ dB}$. The bandwidth strongly depends on the gradient. For low gradients (in red), the lower cutting frequency is not reachable due to the resolution of the frequency step, which means that most of signals are not filtered. The larger the gradient, the smoother the filter: the bandwidth becomes larger but it does not impact the estimation, since the relative perturbation $\Delta\lambda/\lambda$ decreases, whereas if λ is smaller, this ratio tends to be very high. Hence, the filter becomes sharper with a very long time constant. The maximal gain H_0^1 is also a function of (λ, v) (Fig. 3).

The bandwidth is presented on Fig. 4. The cutting frequencies reported to the velocity are functions of λv^{-2} . The model for the lower frequency can hardly be identified for small λ or v , due to the lack of observability of the system: the magnitude of the second order kernel is smaller

¹ The band-pass nature of the filter is due to signal digitalization: the gain at $f = 0 \text{ Hz}$ glues with the gain at the Shannon frequency $f = f_{\text{sh}} = 1/(2\Delta t)$ since a discretized Bode plot is a f_{sh} -periodic function.

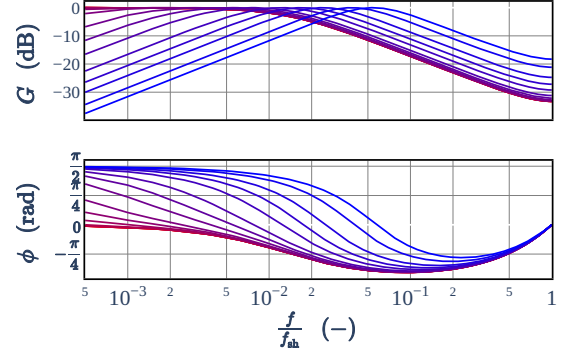


Fig. 2. Bode plots for a range of magnetic gradients λ from $1 \text{ mG} \cdot \text{m}^{-1}$ in red to $50 \text{ G} \cdot \text{m}^{-1}$ in blue – with a displacement velocity of $0.5 \text{ m} \cdot \text{s}^{-1}$.

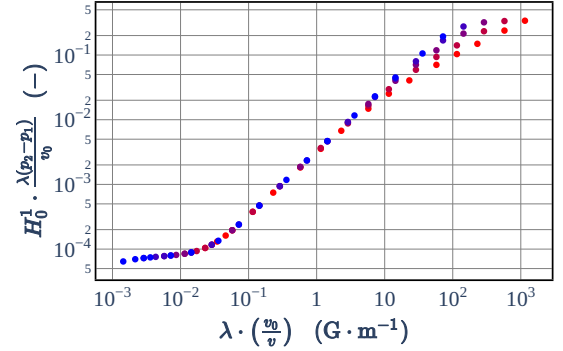


Fig. 3. Gain H_0^1 for a velocity range from $0.25 \text{ m} \cdot \text{s}^{-1}$ in red to $4 \text{ m} \cdot \text{s}^{-1}$ in blue, and different gradients.

in magnitude compared with the noise of the amplitude of the perturbation, so the signal-to-noise ratio (SNR) of this second-order perturbation is very low and this kernel can not be identified. Yet, the upper frequency is fully modeled, with a plateau for low λ/v , which can be explained by the settings of the Kalman filter: the relative ratio $\Delta\lambda/\lambda$ is equivalent to the noise process of the filter.

4.4 Computation of a Bode plot with Monte-Carlo

For LTI systems, Bode plots can be experimentally computed by analyzing the response of the system to diverse frequencies, since LTI systems are theoretically independent of the phase and the amplitude of the input. Therefore, the Bode plots of the linearized MIDR-EKF can be identified by testing several inputs with different frequencies in Monte-Carlo simulations. However, this method is very greedy and requires many more computations than a kernel identification. Furthermore, the identification of the gain requires to determine the peaks in the Discrete Fourier Transforms, which is numerically very sensitive to the convolution window (Rockwood and Erve (2014)), and to spectral leakage (Harris (1978)). The cutting frequencies identified by Monte-Carlo simulations are presented in black stars on Fig. 4. Only one simulation is at 1% consistent with the kernel-based model. This shows that

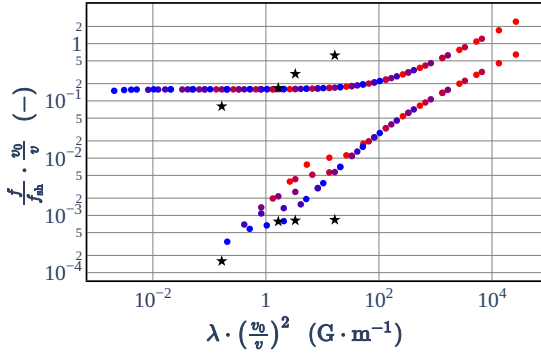


Fig. 4. The bandwidth ($f_{\text{low}}, f_{\text{up}}$) as a function of (v, λ) for a velocity range from $0.25 \text{ m} \cdot \text{s}^{-1}$ in red to $4 \text{ m} \cdot \text{s}^{-1}$ in blue. Monte-Carlo results are shown in black stars.

this brute-force method is not reliable and not consistent for complex systems such as EKF.

4.5 A suitable bandwidth for indoor navigation

The MIDR-EKF is mostly used for pedestrian navigation, and should preserve the magnetic variations due to the movement of the operator and filter all the perturbations that disturb the navigation. With the settings of the MIMU, the upper plateau is around $(f v_0)/(f_{\text{sh}} v) \approx 0.18$, *i.e.* $\sim 9 \text{ Hz}$. For instance, a regular walk is around 1 to 2 Hz, which is inside the bandwidth: the motion is saved by the filter. Moreover, indoor navigation can be perturbed by power line interferences, which induces electromagnetic alternating signals at 50 Hz in Europe or 60 Hz in America. These frequencies are hence naturally filtered. Other high frequency phenomena, *e.g.* opening doors or electromagnetic pulses, are also filtered.

5. VALIDATION WITH 3 DIMENSIONAL SIMULATION

We now validate our 1D model with 3D trajectories. Since we need controlled constant magnetic gradient and velocities, we require numerical simulations for validation.

5.1 Set Up of the simulations

We model a 3D linear magnetic field $\mathbf{B}^n(\mathbf{x}^n) = \mathbf{B}_0^n + \nabla \mathbf{B}_0^n \mathbf{x}^n$ in the navigation frame with $\mathbf{B}_0^n = (0, 0.15, 0.45)^\top \text{ G}$ and $\nabla \mathbf{B}_0^n = \text{diag}(0.05, 0.01, -0.06) \text{ G} \cdot \text{m}^{-1}$. This traceless symmetric gradient satisfies to Maxwell's equation (Neymann et al. (2023a)). Since a nonrotative motion is assumed, navigation and body frames are identical so the upperscripts (n) and (b) drop out. The trajectory is assumed to be towards the line $\Delta = \{(x, 0, 0)^\top, x \in \mathbb{R}\}$, on which a constant magnetic gradient $\lambda = 0.05 \text{ G} \cdot \text{m}^{-1}$ is applied, and the motion is uniform *s.t.* $\dot{x} = v$. All the N 3D-magnetometers are disturbed with the same gaussian noise $\mathcal{N}(0, \sigma_{\text{mag}}^2)$. With a symmetric geometry of the array, the resulting average sensor has also a gaussian noise $\Delta M \sim \mathcal{N}(0, \sigma_{\text{mag}}^2/N)$. The simulations were run on 180 s and the perturbations were added in the magnetic data after the filter reaches its steady state regime.

Table 1. Relative upper bounds of the perturbation in the estimation of the velocity (in %) for different velocities and $n = 20$ simulations, compared with the prediction of the model.

Simulation	$v = 0.25 \text{ m} \cdot \text{s}^{-1}$	$v = 0.50 \text{ m} \cdot \text{s}^{-1}$
1	0.120 %	0.066 %
2	0.084 %	0.109 %
3	0.105 %	0.079 %
4	0.084 %	0.091 %
5	0.077 %	0.112 %
6	0.081 %	0.065 %
7	0.114 %	0.070 %
8	0.089 %	0.075 %
9	0.081 %	0.072 %
10	0.094 %	0.121 %
11	0.106 %	0.071 %
12	0.102 %	0.118 %
13	0.120 %	0.112 %
14	0.101 %	0.097 %
15	0.096 %	0.100 %
16	0.103 %	0.071 %
17	0.090 %	0.090 %
18	0.096 %	0.092 %
19	0.089 %	0.090 %
20	0.122 %	0.090 %
Maximum	0.122 %	0.121 %
Average	0.098 %	0.090 %
Uncertainty	$\pm 0.009 \%$	$\pm 0.012 \%$
Model	0.390 %	0.105 %

5.2 Assessment of the performance

The velocity error $\Delta v_k = \hat{v}_k - \bar{v}$ is processed for each simulation. Notice that \hat{v}_k is as the best estimation of the state by a Kalman filter already an expected value. The assessment of the performance relies on Theorem 1. Recalling that $h^0 = 0$ and that h^2 were negligible, we have, for a disturbance ΔM , $\|\Delta v\|_\infty \leq \|h^1\|_1 \|\Delta M\|_\infty$. The value of $\|h^1\|_1$ is especially given by the knowledge of this kernel thanks to Fig. 2 and 3. In our case, we have at 99.73%, $\|\Delta M\|_\infty \approx 3\sigma_{\text{mag}}/\sqrt{N}$, *i.e.* $\|\Delta v\|_\infty \leq \|h^1\|_1 \cdot 3\sigma_{\text{mag}}/\sqrt{N}$. The average value $\overline{\|\Delta v\|_\infty}$ of $\|\Delta v\|_\infty$ is evaluated over a series of $n = 20$ simulations. The uncertainty around this average value is quantified at 99.73% as $3\hat{\sigma}_n/\sqrt{n}$, where $\hat{\sigma}_n = \sqrt{n/(n-1) \cdot \text{Var}(\|\Delta v\|_\infty)}$ is the unbiased estimator of the standard deviation. In particular, we verify that

$$\overline{\|\Delta v\|_\infty} + 3\hat{\sigma}_n/\sqrt{n} \leq \|h^1\|_1 \cdot 3\sigma_{\text{mag}}/\sqrt{N}. \quad (12)$$

5.3 Results

The assessment of the relative error $\overline{\|\Delta v\|_\infty}/v$ over all the simulations and the identification uncertainty for $v = 0.25 \text{ m} \cdot \text{s}^{-1}$ and $0.50 \text{ m} \cdot \text{s}^{-1}$ are displayed on Table 1. Considering the uncertainty interval around the estimated average, the simulated upper bound $\overline{\|\Delta v\|_\infty}/v$ is consistent with the inequality (12) for each batch of simulations. Yet, the model is less efficient for $v = 0.25 \text{ m} \cdot \text{s}^{-1}$ than for $v = 0.50 \text{ m} \cdot \text{s}^{-1}$, with an overestimated upper bound 3 times larger than the simulated value.

6. CONCLUSION

In this paper, the bandwidth of a MIDR-EKF was determined up to the hardware constants and to the navigation

scenario. We relied on a 1D toy-model of the system and linearized the equations to highlight a SISO transfer from magnetic disturbances to the velocity and to identify the BLA of this latter. We proved that, under some conditions, the result extends to any EKF through the derivation of a LTI transfer matrix. We showed the consistency of this result with the decomposition in Volterra kernels, and derived an abacus of the bandwidth with respect to the navigation scenario. The analysis of the bandwidth of the MIDR-EKF emphasized that this algorithm is suitable for indoor navigation and naturally filters some unmodeled outliers. Finally a validation with 3D simulations proved that this model was reliable and statistically consistent in realistic use case situations. As a future research, some attention should be paid to understand how the navigation scenario impacts the gain and the bandwidth, *e.g.* through a computation of the LTI transfer matrix. Furthermore, some phenomena, *s.t.* noise aliasing, still remain unmodeled. Experiments with real-life data should also be done.

REFERENCES

- Anderson, B. and Moore, J. (1979). *Optimal Filtering*. Dover Publications, Inc., New York.
- Birpoutsoukis, G., Csurcsia, P., and Schoukens, J. (2018). Efficient multidimensional regularization for Volterra series estimation. *Mechanical Systems and Signal Processing*, 102, 896–914. doi:2017.10.0070888-3270.
- Birpoutsoukis, G., Marconato, A., Lataire, J., and Schoukens, J. (2017). Regularized nonparametric Volterra kernel estimation. *Automatica*, 82, 324–327. doi: http://dx.doi.org/10.1016/j.automatica.2017.04.014.
- Bouvier, D., Hélie, T., and Roze, D. (2017). Homophase signal separation for Volterra series identification. *20th International Conference on Digital Audio Effects*. doi: 10.1109/CDC.2018.8619740.
- Boyd, S. and Chua, L. (1985). Fading memory and the problem of approximating nonlinear operators with Volterra series. *IEEE*.
- Chesneau, C.I., Hillion, M., and Prieur, C. (2016). Motion estimation of a rigid body with an EKF using magnetoinertial measurements. *2016 International Conference on Indoor Positioning and Indoor Navigation (IPIN)*.
- Chesneau, C.I., Robin, R., Meier, H., Hillion, M., and Prieur, C. (2019). Calibration of a magnetometer array using motion capture equipment. *Asian Journal of Control*, 1459–1469. doi:hal-02368023.
- Harris, F. (1978). On the use of windows for harmonic analysis with the discrete Fourier transform. *Proceedings of the IEEE*, 66(1), 51–83. doi:hal-02368023.
- Neymann, R., Berthou, A., Jourdas, J.F., Lhachemi, H., Prieur, C., and Girard, A. (2023a). Magneto-inertial dead-reckoning navigation with walk dynamic model in indoor environment. *13th International Conference on Indoor Positioning and Indoor Navigation (IPIN)*.
- Neymann, R., Meier, H., Lhachemi, H., Prieur, C., and Girard, A. (2023b). Minimization of parameter sensitivity to pre-estimation errors and its application to the calibration of magnetometer arrays. *European Control Conference (ECC)*.
- Radix, J.C. (1993). *Systèmes Inertiels à Composants Liés "Strap-Down"*. Cépaduès Editions, Ecole Nationale Supérieure de l'Aéronautique et de l'Espace.
- Rockwood, A. and Erve, J. (2014). Mass spectral peak distortion due to Fourier transform signal processing. *Journal of the American Society for Mass Spectrometry*, 25(12), 2163–2176. doi:doi:10.1155/2010/967245.
- Rugh, W. (1981). *Nonlinear System Theory. The Volterra/Wiener Approach*. The Johns Hopkins University Press, ISBN O-8018-2549-0e.
- Schetzen, M. (1980). *The Volterra and Wiener Theories of Nonlinear Systems*. Wiley, New York.
- Schoukens, J. and Ljung, L. (2019). Nonlinear system identification. *IEEE Control System Magazine*, 28–99. doi:10.1109/MCS.2019.2938121.
- Schoukens, M. and Tiels, K. (2017). Identification of block-oriented nonlinear systems starting from linear approximations: A survey. *Automatica*, 85, 272–292. doi: 2017.06.0440005-1098.
- Vissière, D., Martin, A., and Petit, N. (2007). Using distributed magnetometers to increase imu-based velocity estimation into perturbed area. *Conference on Decision and Control (CDC)*, 4924–4931.
- Zmitri, M., Fourati, H., and Prieur, C. (2021). Magnetic field gradient-based EKF for velocity estimation in indoor navigation. *Sensors*, 572. doi:10.3390/s20205726.

Appendix A. PROOF OF THEOREM 2

Let $\hat{\mathbf{x}}_k = \hat{\mathbf{x}}_{k|k}$ be the estimated state of an actual quantity $\bar{\mathbf{x}}_k = \bar{\mathbf{x}}_{k|k}$, which are ruled by the following dynamics:

$$\begin{aligned}\hat{\mathbf{x}}_{k+1} &= \mathbf{F}_k \hat{\mathbf{x}}_k + \mathbf{G}_k \mathbf{u}_k \\ &\quad + \mathbf{K}_{k+1} (\mathbf{z}_{k+1} - \mathbf{H}_k \mathbf{F}_k \hat{\mathbf{x}}_k - \mathbf{H}_k \mathbf{G}_k \mathbf{u}_k) \\ \bar{\mathbf{x}}_{k+1} &= \bar{\mathbf{F}}_k \bar{\mathbf{x}}_k + \bar{\mathbf{G}}_k \mathbf{u}_k,\end{aligned}$$

where $\mathbf{F}_k = \bar{\mathbf{F}}_k + \Delta \mathbf{F}_k$ and $\mathbf{G}_k = \bar{\mathbf{G}}_k + \Delta \mathbf{G}_k$. By subtracting $\hat{\mathbf{x}}_{k+1}$ to $\bar{\mathbf{x}}_{k+1}$, it comes

$$\begin{aligned}\hat{\mathbf{x}}_{k+1} - \bar{\mathbf{x}}_{k+1} &= \mathbf{F}_k (\hat{\mathbf{x}}_k - \bar{\mathbf{x}}_k) + \Delta \mathbf{F}_k \bar{\mathbf{x}}_k + \Delta \mathbf{G}_k \mathbf{u}_k \\ &\quad + \mathbf{K}_{k+1} (\mathbf{z}_{k+1} - \mathbf{H}_k \mathbf{F}_k \hat{\mathbf{x}}_k - \mathbf{H}_k \mathbf{G}_k \mathbf{u}_k) \\ &= \mathbf{F}_k \Delta \hat{\mathbf{x}}_k + \Delta \mathbf{F}_k \bar{\mathbf{x}}_k + \Delta \mathbf{G}_k \mathbf{u}_k \\ &\quad + \mathbf{K}_{k+1} (\mathbf{z}_{k+1} - \mathbf{H}_k \mathbf{F}_k \hat{\mathbf{x}}_k - \mathbf{H}_k \mathbf{G}_k \mathbf{u}_k).\end{aligned}$$

The differentiation of the propagation equation around the truth $\bar{\mathbf{x}}_k$ and \mathbf{u}_k yields

$$\begin{aligned}\mathbf{F}_k \hat{\mathbf{x}}_k &= \mathbf{H}_k \bar{\mathbf{F}}_k \bar{\mathbf{x}}_k - \mathbf{H}_k \Delta \mathbf{F}_k \bar{\mathbf{x}}_k - \mathbf{H}_k \mathbf{F}_k (\hat{\mathbf{x}}_k - \bar{\mathbf{x}}_k) \\ \mathbf{G}_k \mathbf{u}_k &= (\bar{\mathbf{G}}_k + \Delta \mathbf{G}_k) \mathbf{u}_k,\end{aligned}$$

which implies

$$\begin{aligned}\hat{\mathbf{x}}_{k+1} - \bar{\mathbf{x}}_{k+1} &= (\mathbf{I} - \mathbf{K}_{k+1} \mathbf{H}_k) [\mathbf{F}_k (\hat{\mathbf{x}}_k - \bar{\mathbf{x}}_k) \\ &\quad + \Delta \mathbf{F}_k \bar{\mathbf{x}}_k + \Delta \mathbf{G}_k \mathbf{u}_k] \\ &\quad + \mathbf{K}_{k+1} (\mathbf{z}_{k+1} - \mathbf{H}_k \bar{\mathbf{F}}_k \bar{\mathbf{x}}_k - \mathbf{H}_k \bar{\mathbf{G}}_k \mathbf{u}_k).\end{aligned}$$

Now, due to $\bar{\mathbf{x}}_{k+1} = \bar{\mathbf{F}}_k \bar{\mathbf{x}}_k + \bar{\mathbf{G}}_k \mathbf{u}_k$, we have

$$\begin{aligned}\hat{\mathbf{x}}_{k+1} - \bar{\mathbf{x}}_{k+1} &= (\mathbf{I} - \mathbf{K}_{k+1} \mathbf{H}_k) [\mathbf{F}_k (\hat{\mathbf{x}}_k - \bar{\mathbf{x}}_k) \\ &\quad + \Delta \mathbf{F}_k \bar{\mathbf{x}}_k + \Delta \mathbf{G}_k \mathbf{u}_k] \\ &\quad + \mathbf{K}_{k+1} (\mathbf{z}_{k+1} - \mathbf{H}_k \bar{\mathbf{x}}_{k+1}).\end{aligned}$$

Finally, we take the expected value of the expression and assume that $\mathbb{E}[\Delta \mathbf{F}_k] = \mathbf{0}$ and $\mathbb{E}[\Delta \mathbf{G}_k] = \mathbf{0}$ and that they are uncorrelated with $\bar{\mathbf{x}}_k$ and \mathbf{u}_k conversely. With $\Delta \mathbf{x}_k = \mathbb{E}[\hat{\mathbf{x}}_k - \bar{\mathbf{x}}_k]$ and $\Delta \mathbf{z}_k = \mathbb{E}[\mathbf{z}_k - \mathbf{H}_k \bar{\mathbf{x}}_k]$, one has:

$$\Delta \mathbf{x}_{k+1} = (\mathbf{I} - \mathbf{K}_{k+1} \mathbf{H}_k) \mathbf{F}_k \Delta \mathbf{x}_k + \mathbf{K}_{k+1} \Delta \mathbf{z}_{k+1}. \quad (\text{A.1})$$